Supporting Information -
Photoelectrochemical behaviour of photoanodes under high photon fluxes

Isaac Holmes-Gentle, Franky E. Bedoya-Lora, Lorenzo Aimone, and Sophia Haussener

S1 Reported literature on high light flux photoelectrochemical devices

Table S1 shows a list of reported photoelectrochemical devices operating under concentrated light. Photoelectrochemical devices can be separated into three categories: 1) "true" photoelectrochemical devices which contain semiconductor-electrolyte junction, 2) devices where the photovoltaic element is separated from the electrochemical, and 3) particulate photoelectrochemistry systems/photo-catalyst. This is denoted in Table S1 as PEC, PV/EC and PC respectively. Some devices have a semiconductor-electrolyte junction biased by a external PV and these are categorised as "PEC" in Table S1.

Table S1: Review of notable experimental PEC cells operating under high solar concentration. Superscripts: † = estimated from reported concentration factor, ‡ = estimated from reported solar cell area and concentrator input area.

Year	First author	Type	Photoabsorber material(s)	Max. concentration (kW m^{-2})	Ref.
1998	Khaselev	PEC	p-GaInP$_2$, GaAs	11.9	[1]
2007	Peharz	PV/EC	GaInP, GaInAs	500	[2]
2008	Wang	PEC	Fe$_2$O$_3$, p-GaInP$_2$	10†	[3]
2011	Ong	PEC	Fe$_2$O$_3$	3.5	[4]
2013	Bell	PC	TiO$_2$	52	[5]
2014	Rau	PV/EC	GaInP, GaInAs	500†	[6]
2014	Shaner	PEC	WO$_3$, Si	12	[7]
2015	Bonke	PV/EC	GaInP, GaAs, Ge	100	[8]
2015	Nakamura	PV/EC	GaInP, GaAs, Ge	23‡	[9]
2015	Ye	PEC	Fe$_2$O$_3$	9	[10]
2016	Jia	PV/EC	GaInP, GaAs, GaInNAsSb	42	[11]
2016	Segev	PEC	Fe$_2$O$_3$	25.6	[12]
2017	Fallisch	PV/EC	GaInP, GaInAs	250‡	[13]
2018	Vilanova	PEC	Fe$_2$O$_3$, Si	17	[14]
2018	Vilanova	PEC	Fe$_2$O$_3$	2.5	[15]
2018	Bicer	PEC	Cu$_2$O, Si	5.8	[16]
2019	Tembhurne	PV/EC	GaInP, GaInAs, Ge	474	[17]
2020	Gupta	PEC	LaFeO$_3$	18	[18]
2020	Khan	PV/EC	GaInP, GaInAs, Ge	207	[19]
2020	Vilanova	PEC	Fe$_2$O$_3$, Si	12.8	[20]
2020	Xing	PC	Au/TiO$_2$	9	[21]
2023	Zhou	PC	InGaN/GaN	160.7	[22]
2023	Holmes-Gentle	PV/EC	GaInP, GaAs, Ge	761	[23]
2023	**Holmes-Gentle**	**PEC**	**Fe$_2$O$_3$, BiVO$_4$**	**359**	**This work**

The results of the literature review shown in Table S1 are visualised in Fig. S1. Previously reported devices that contain a semiconductor-electrolyte junction have been tested at less than 30 suns. In this work, the experimental irradiance achieved was an order of magnitude higher than previous PEC experiments and was in a similar range to devices which employ a concentrated photovoltaic cell based on III-V semiconductors.
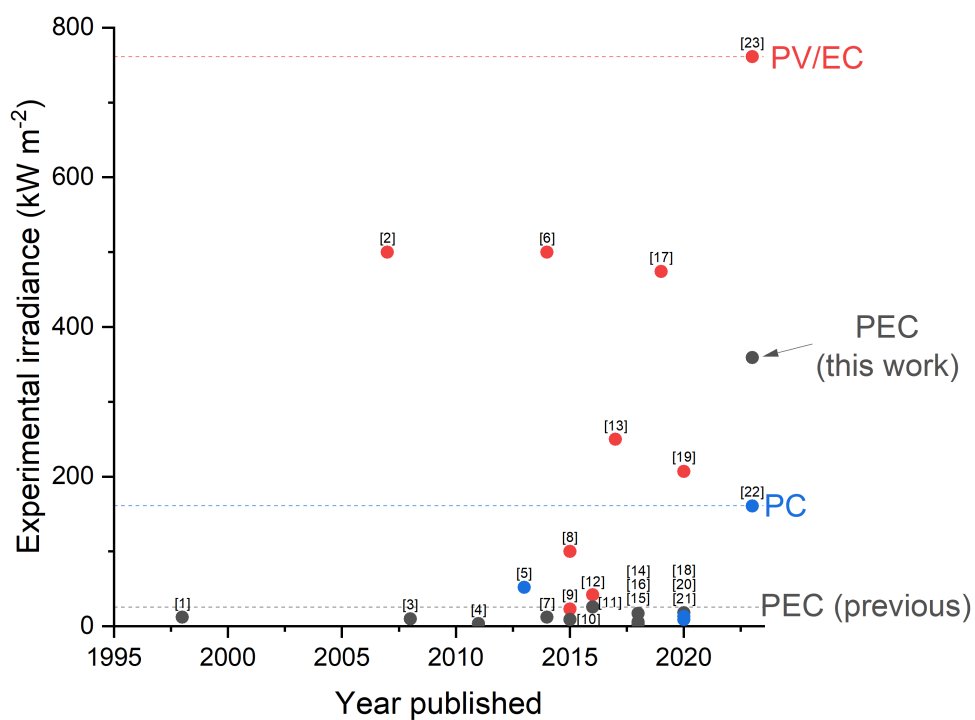

Figure S1: A review of notable experimental PEC cells operating under high solar concentration. Device type is denoted by colour (grey = PEC, red = PV/EC). The PEC experiments described in this work are highlighted in blue.

S2 Additional methodology

S2.1 Experimental overview

The High Flux Solar Simulator (HFSS), located at the EPFL Lausanne Campus, can simulate concentrated sunlight at various levels of light intensity. The HFSS is comprised of $18\times$ 2.5 kW$_e$ short-arc xenon lamps, each one coupled with an ellipsoidal mirror (for more information, see Bader *et al.* [24], Levêque *et al.* [25]). The intensity of the concentrated sunlight can be modulated by the current intensity of each lamp, the number of lamps in use and the position of the experiment relative to the HFSS lamps. In this experimental campaign, one single lamp operating at a fixed current of 90 A was used and the irradiance was varied only *via* positioning of experiment on the servomotor-actuated optical table. Figure S2 shows the experimental setup mounted in the HFSS.
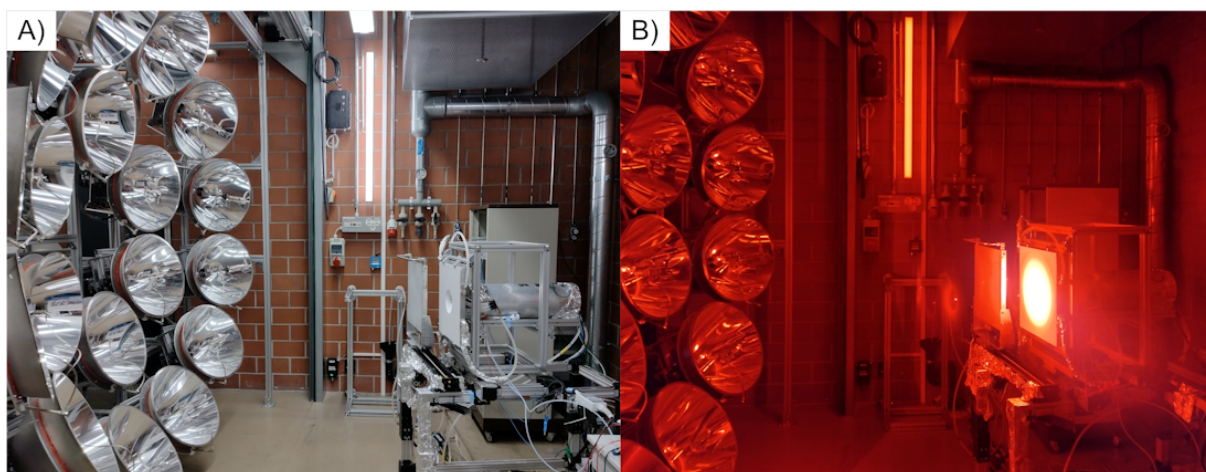

Figure S2: Photographs of the HFPEC experiments at the HFSS facility where a) system during setup (no light) and b) system during operation (light turned on). The red colour comes from the protective glass between the control room and the experimental room.

The experimental setup, as described further in the main text, comprised of an electrolyte reservoir, pump and a high-flux photoelectrochemical test cell connected to a potentiostat. The light is produced by a Xe-bulb lamp with an ellipsoidal reflector and passes through an aperture/light shield. A schematic of the experimental setup is shown Fig. S3. Figure S4 shows a photograph of the partially disassembled HFPEC cell.
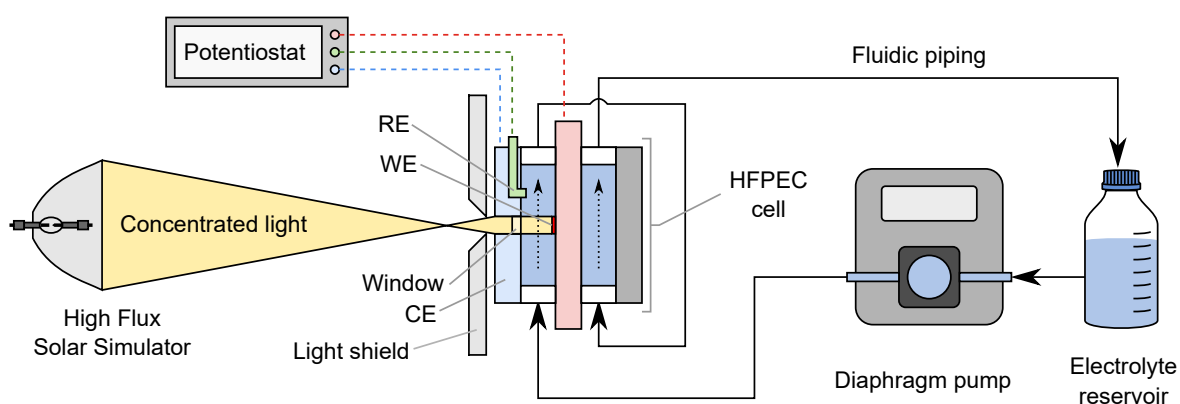

Figure S3: Overview of experimental setup with each key component labelled.
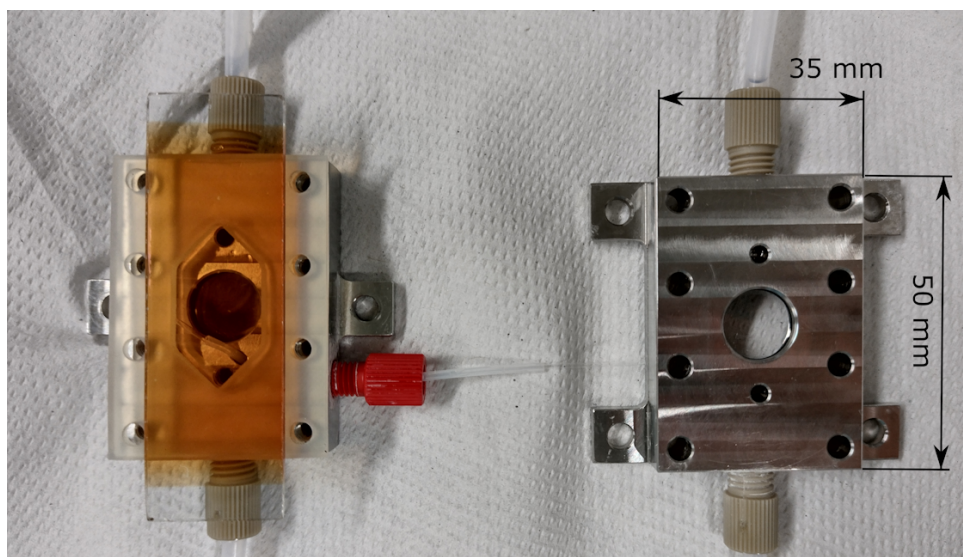
Figure S4: Photograph of the disassembled HFPEC cell showing the end plate and an example Fe_2O_3|FTO photoelectrode.

S2.2 Sn-doped hematite synthesis

Prior the deposition of the films, the substrates were thoroughly cleaned. In the case of FTO, the samples were ultrasonicated for 15 min in DI water with soap, acetone, ethanol and water, in that order, and dried with a stream of nitrogen. For Ti substrates, the samples were immersed in 0.5 M oxalic acid overnight, then washed with abundant water and ethanol, and drying with nitrogen.

Sn-doped Fe_2O_3 was synthesised *via* spray pyrolysis as reported by Bedoya-Lora *et al.*[26] A solution comprised of 0.1 M $FeCl_3.6H_2O$ (>99%, Acros Organics) and 0.6 mM $SnCl_4$ (anhydrous, 99%, Thermo Fisher Scientific) in ethanol (99.8% Fisher Chemical) was sprayed on heated substrates. The precursor was nebulised with a quartz spray nozzle (Meinhard, USA) at a height of 150 mm above the surface of the substrate, which was kept at 450 °C. 20 passes and 40 passes of precursor flowing at 2 $cm^3\,min^{-1}$ were sprayed onto FTO (13 Ω/sq, Solaronix TC22-15, 2 mm) and titanium foil (0.127 mm, 99.7%, Sigma-Aldrich), respectively. A 60 second rest between passes was necessary to allow the precursor to evaporate completely. The samples were then annealed at 400 °C for 1 h in air. Sn doping concentration was *ca.* 0.6% by mol and 1.3% by mass respect to Fe.

S2.3 Bismuth vanadate synthesis

Similarly, $BiVO_4$ photoelectrodes were fabricated *via* spray pyrolysis following the procedure reported by Abdi *et al.*[27] First, a layer of SnO_2 was deposited on FTO. 5 layers of Sn precursor, 0.1 M $SnCl_4$ (anhydrous, 99%, Thermo Fisher Scientific) in ethyl acetate (99.5% Merck) were sprayed on FTO (13 Ω/sq, Solaronix TC22-15, 2 mm) at 425 °C at a rate of 6 $cm^3\,min^{-1}$ with 60 s wait between layers. Next, 62 layers of Bi and V precursor, 8 mM $Bi(NO_3)_2$ (98%, Carl Roth) + 8 mM $VO(AcAc)_2$ (99%, Thermo scientific) in a solution of acetic acid (99.7% Fisher Scientific) : ethanol (99.8% Fisher Chemical) (50:450 volume), were sprayed onto FTO|SnO_2 at 450 °C at a rate of 6 $cm^3\,min^{-1}$ with 60 seconds wait between layers. The samples were annealed at 450 °C for 2 h in air.

S2.4 HFSS operation and light flux calibration

The high flux solar simulator (HFSS) was operated with a single lamp (id = #3) at a current of 90 A. After ≈ 10 minutes stabilisation, the amount of light received by the target was calibrated via two methods to obtain optical table positions (controlled with servomotor-actuated lead screw positioning system) for various solar concentrations between 37-359 kW m^{-2}. Firstly, the light intensity and flux distribution was assessed with CCD-camera images of a flux gauge calibrated 'Lambertian' target at various optical table position.[25]

This first evaluation of the flux was then followed by a more accurate calibration of the amount of light passing through the HFPEC shield/aperture *via* calorimetry following the methodology of Gill *et al.*[28]. Photographs of the calorimeter and experimental setup can be found in Fig. S5. For each optical table position, the incident power absorbed was measured by performing an energy balance on the cooling water flowing through the calorimeter at steady-state. Measurements were performed at a constant flow rate of the cooling water. Specific heat capacity of water was assumed constant due to the low range of temperatures observed (maximum temperature difference between inlet and outlet of approximately 2°C). PT100 1/10 DIN "class B" were used to measure the water temperature ensuring an accuracy of ±0.03°C.
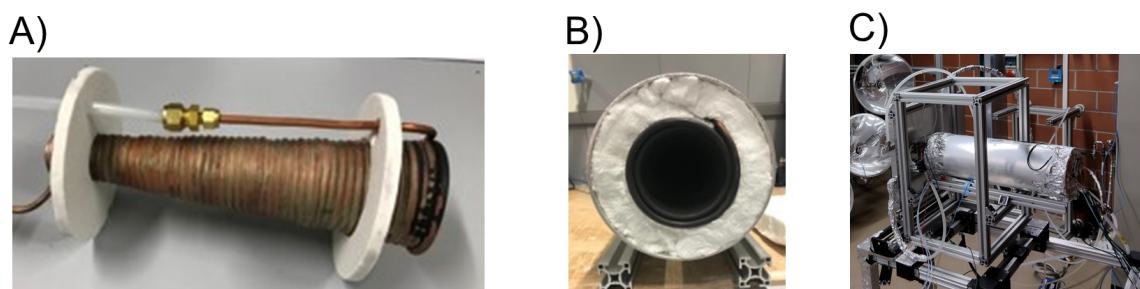

Figure S5: Photographs of HFSS calorimeter showing a) Internal water cooled cavity, b) entrance of internal cavity, and c) the complete experimental setup

The amount of light received by the high flux PEC cell at the plane of the sample was assessed primarily through the use of a water-cooled calorimeter, the results of which can be found in Table S2. To calculate the the light irradiance at the sample, the total light power that passed through the aperture was divided by the illuminated sample area. Due to the non-collimated light source, this area depended on optical table position. The sample area was estimated from the $BiVO_4$ degradation patterns, as shown in Fig. S6, after the chronoamperometry experiments at various light flux intensities.

Table S2: Results of the calorimeter calibration and measurement of illuminated area from degraded $BiVO_4$ samples. Here, Z and Y are the table position where $Z = 0$ is approximately the focal plane and $Y = 0$ is the approximately the position of the peak of the irradiance.

Z	Y	Power (Calorimeter)	Illuminated area	Equivalent diameter	Light Irradiance (Calorimeter)	Light Irradiance (Flux mapping)
cm	cm	W	mm^2	mm	kW m^{-2}	kW m^{-2}
0	0	14.24	39.7	7.11	358.5	384.3
5	0	10.26	35.4	6.71	290.1	298.0
10	0	7.075	30.8	6.26	229.5	208.7
15	0	4.62	26.7	5.84	172.8	131.4
22	0	2.82	23.1	5.42	122.2	85.5
22	3	1.62	19.0	4.92	85.3	70.0
22	5	0.56	15.1	4.39	37.3	28.4

The light power passing through the aperture was also assessed by integrating the irradiance over the aperture area from the flux mapping experiments using the lambertian target and a calibrated camera. Figure S7a shows good agreement of the integrated power from the flux mapping method when compared to the calorimeter results. However, due to the high degree of inaccuracy of the flux mapping method for assessing the amount of through a small aperture, the calorimeter results where used in this work. This uncertainty comes from a limited number of pixels for integration (from small size of the 5 mm diameter aperture combined with the camera resolution and positioning) and the sensitivity to small positioning errors as the experiments require the careful alignment of the lambertian target and the flux gauge target during the calibration process of the camera. These challenges can be illustrated in Fig. S7b, which shows the scale of the flux target relative to the aperture and concentrated light beam.
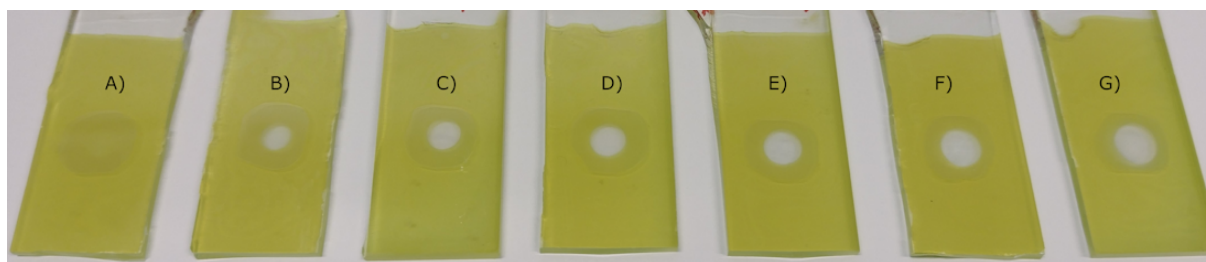
Figure S6: Degradation patterns of BiVO$_4$ under various illumination concentrations: a) 37.3 b) 85.3 c) 122.2 d) 172.8 e) 229.5 f) 290.1 g) 358.5 kW m^{-2}, after 30 minutes of photoelectrolysis at 1.23 V *vs.* RHE
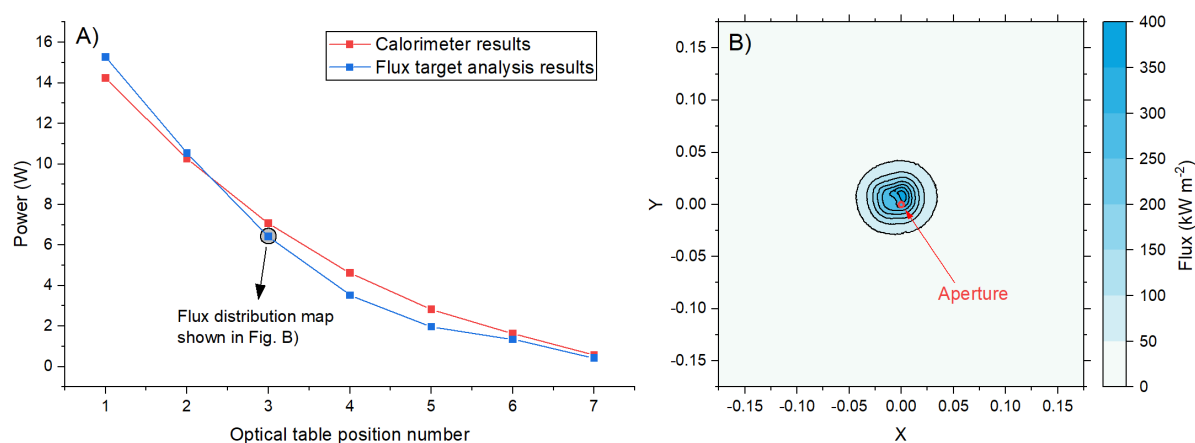

Figure S7: Comparison of HFSS calibration methods. a) The total light power passing through the aperture as assessed by two methods: calorimetry and flux mapping. b) The flux map at optical table position corresponding to a 229.5 kW m-2 flux on the irradiated sample based on the calorimeter results. The plotted area corresponds to the flux target size (35 × 35 cm) and the area and position of the 5 mm diameter aperture is highlighted in red.

Finally, the light spectra was assessed using a UV-vis spectrometer (Ocean optics) placed far out of focal point and the results are shown in Fig. S8. The spectra was normalised to the AM1.5G to allow relative comparison and it was observed that the lamps produce a larger fraction of short-wave UV and near-infrared light in comparison with AM1.5G.
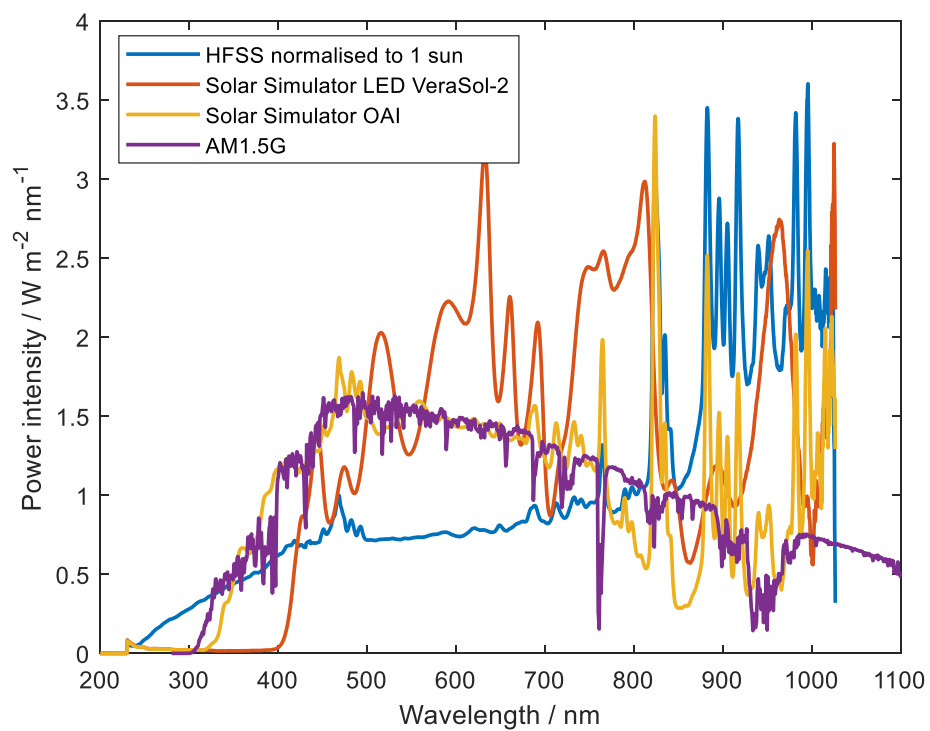
Figure S8: Light sources spectra of the different light sources used in this study. The spectra of the HFSS lamp was normalised respect to AM1.5G by integrating the irradiance between 200 nm and 1000 nm

S2.5 Ohmic drop compensation

The ohmic drop compensation was completed in post-processing due to the limitations of potentiostat for in-situ ohmic drop compensation with large set high resistances according to eq. (1). The uncompensated resistance R_u was composed of two parts: electrolyte resistance R_e and substrate resistance R_s. An electrical diagram highlighting the resistances that are to be corrected for is shown in Fig. S9. Typically, ohmic drop compensation only considers the electrolyte contribution as the substrate resistance is negligible. However, for both substrates considered in this work, this uncompensated resistance is non-negligible (e.g. FTO substrate = 35.5 Ω, Ti substrate = 0.8-1.1 Ω, as measured by electrochemical impedance spectroscopy) and was measured by electrochemical impedance spectroscopy.

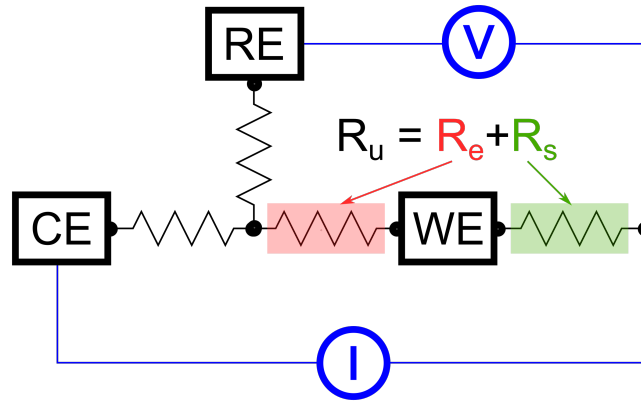$$U_{effective} = U_{applied} - IR_u \tag{1}$$

Figure S9: Equivalent circuit diagram of the three-probe configuration where WE = working electrode, CE = counter electrode, and RE = reference electrode. The uncompensated resistance R_u is shown as the summation of the electrolyte resistance (between RE and WE) R_e and the substrate resistance R_s.

S2.6 Onset potential calculation

We define the onset potential as the potential when the rate of change of photocurrent density with potential exceeds a threshold value (= $20\,\mathrm{A\,m^{-2}\,V^{-1}}$). This is defined differently in the work of Segev et al. [12], as the measured dark current was very low or slightly negative in that region meaning a threshold based on a photocurrent higher than 5 times the dark current gives poor results.

$$E_{\mathrm{onset}} = E\left(\frac{dj_{\mathrm{photo}}}{dE} = 20\,\mathrm{A\,m^{-2}\,V^{-1}}\right) \tag{2}$$

S3 Additional results

S3.1 SEM/EDX images
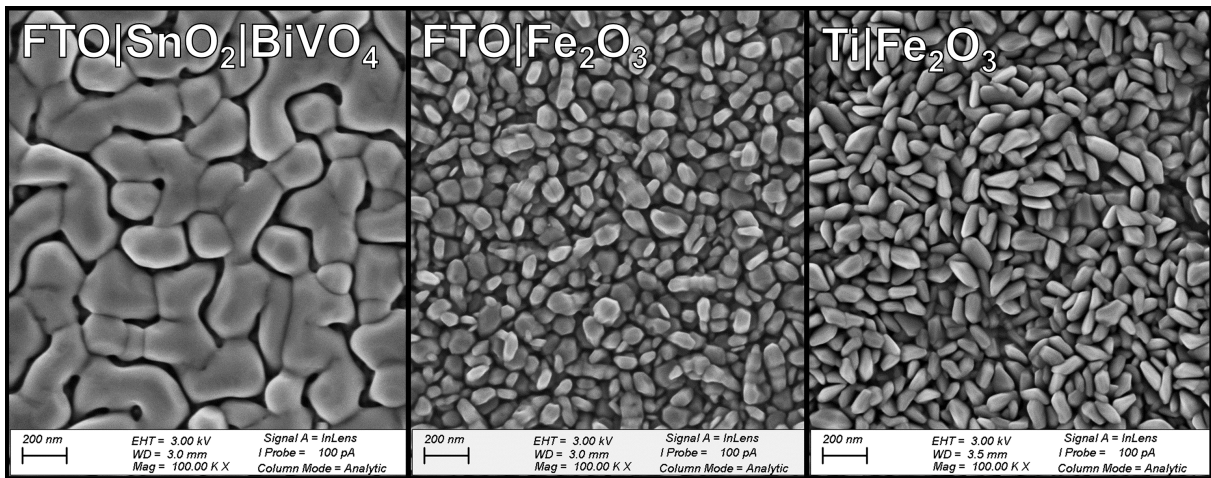
Figure S10: SEM images of pristine surfaces of samples FTO|SnO$_2$|BiVO$_4$, FTO|Fe$_2$O$_3$ and Ti|Fe$_2$O$_3$
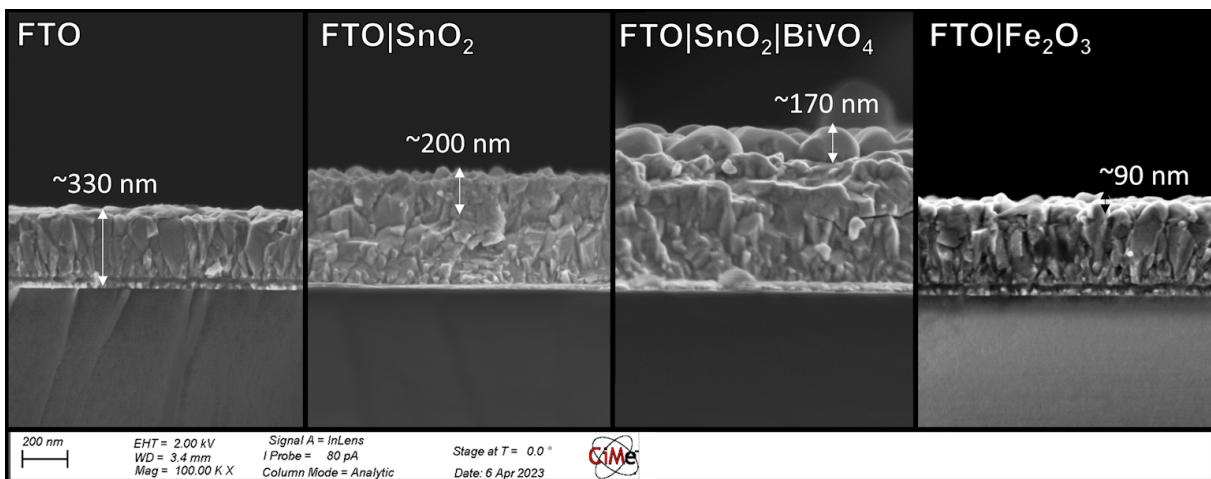

Figure S11: SEM cross section images of pristine surfaces of samples FTO, FTO|SnO$_2$, FTO|SnO$_2$|BiVO$_4$ and FTO|Fe$_2$O$_3$, with respective estimated thicknesses
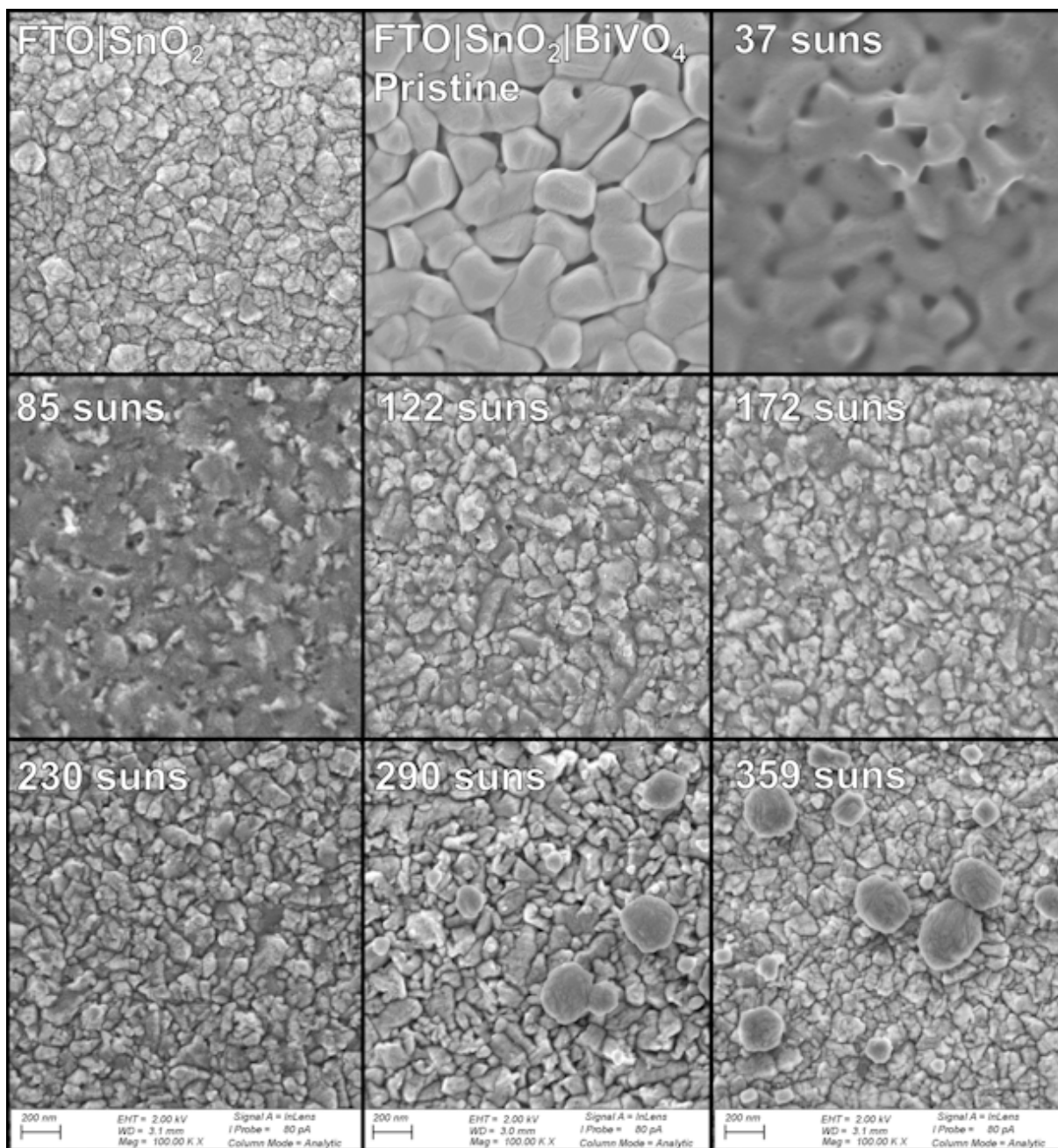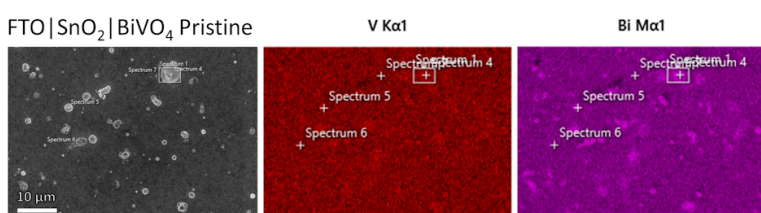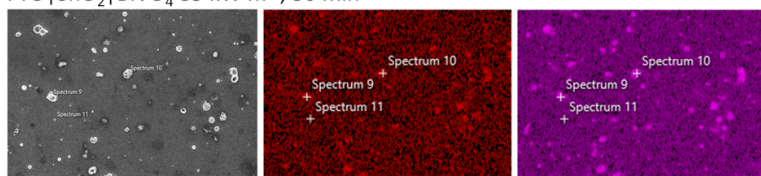
Figure S12: SEM images of FTO|SnO$_2$ and FTO|SnO$_2$|BiVO$_4$ before and after high irradiation for 30 minutes for water splitting at 1.23 V *vs.* RHE
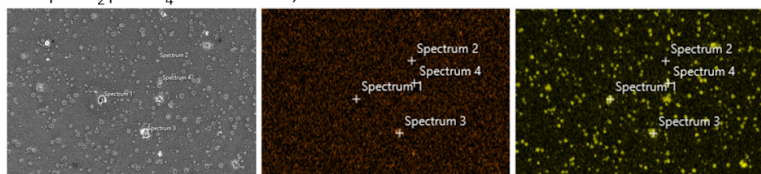
FTO|SnO$_2$|BiVO$_4$ Pristine

V Kα1

Bi Mα1

Element	Atomic %	
	Film (Spectrum 6)	Defect (Spectrum 5)
O	61.22	61.89
V	13.23	17.96
Sn	13.49	2.17
Bi	12.06	17.98
Total:	100	100

FTO|SnO$_2$|BiVO$_4$ 85 kW m^{-2}, 30 min

Element	Atomic %	
	Film (Spectrum 11)	Defect (Spectrum 9)
O	61.56	48.76
Si	0.09	0.46
V	0.95	22.70
Sn	36.57	2.78
Bi	0.84	25.31
Total:	100	100

FTO|SnO$_2$|BiVO$_4$ 358 kW m^{-2}, 30 min

Element	Atomic %	
	Film (Spectrum 2)	Defect (Spectrum 1)
O	70.42	62.81
Si	0.14	0.38
P	N/D	12.04
K	N/D	3.16
V	N/D	3.45
Sn	29.44	3.22
Bi	N/D	14.93
Total:	100	100.00

Figure S13: Elemental analysis *via* EDX of FTO|SnO$_2$|BiVO$_4$ before and after exposure under high irradiation for 30 minutes for water splitting at 1.23 V *vs.* RHE
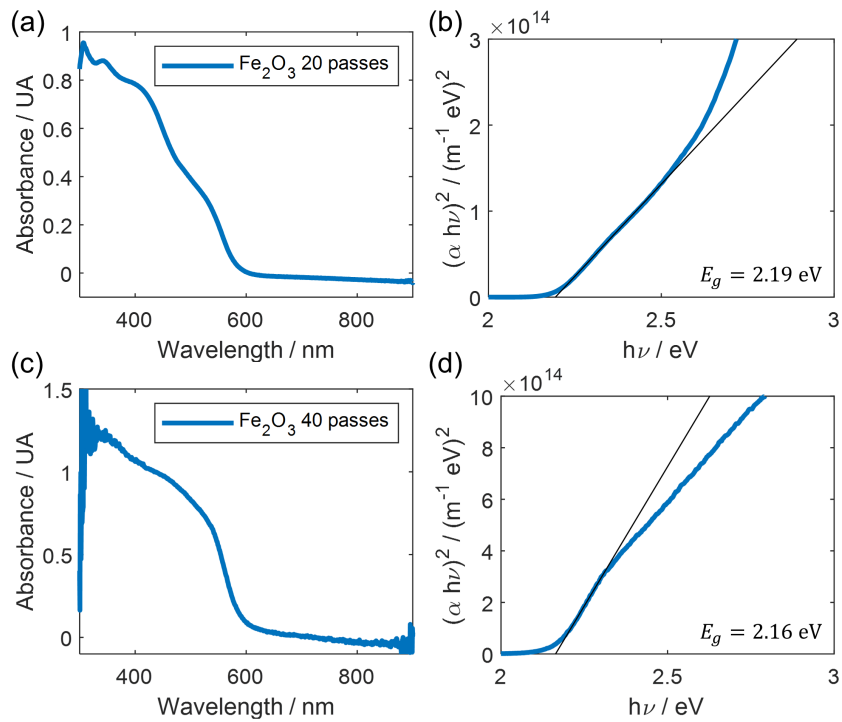
S3.2 Absorbance spectra and band gap

Figure S14: (a,c) Absorbance spectra and (b,d) Tauc plot for direct band gap for FTO|Fe$_2$O$_3$ produced with 20 and 40 passes of spray, respectively.
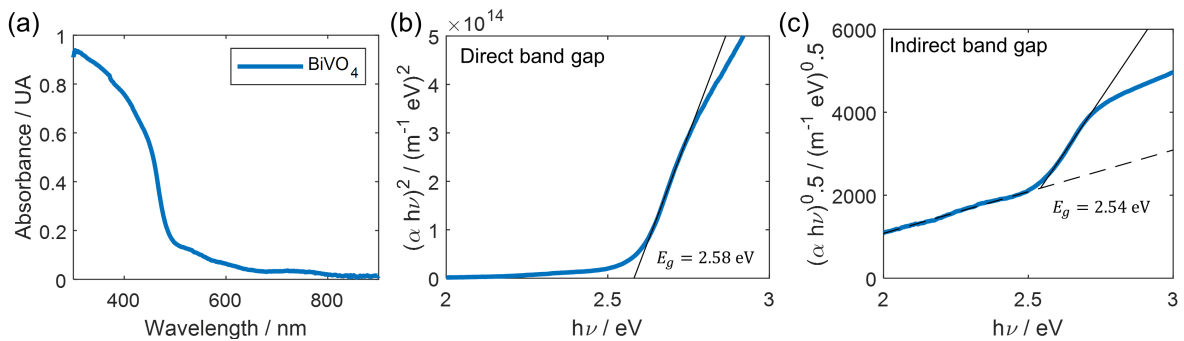

Figure S15: (a) Absorbance spectra, (b) Tauc plot for direct band gap, and (c) Tauc plot for indirect band gap for FTO|BiVO$_4$ photoelectrode.

S3.3 Temperature of photoelectrodes under high irradiance

In order to measure the temperature of the photoelectrodes, four K-type thermocouples were attached to the back of the Ti substrate in four different positions using silver paste and aluminium foil tape as shown in Fig. S16. The temperature of the electrolyte was also measured using thermocouples at different positions throughout the setup (inlet, mid-cell, outlet and bottle). Fig. S17 shows the measured temperatures as a function of time. Irradiances were increased every 10 minutes, and final temperatures were averaged for the last two minutes for each irradiance.
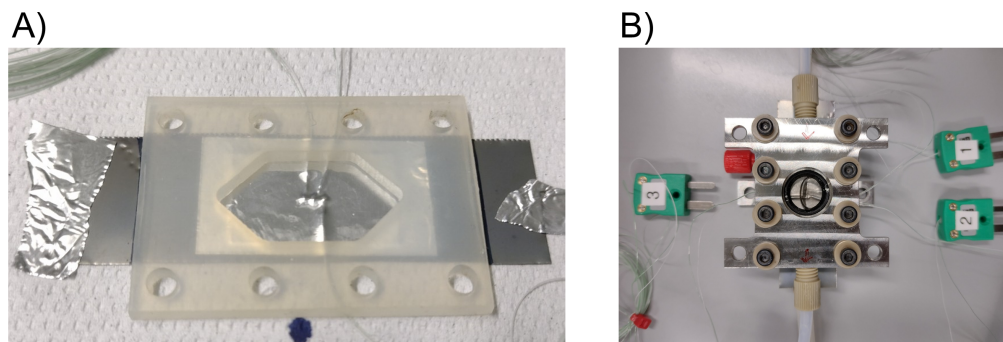

Figure S16: Images of the experimental setup for assess the sample temperature under illumination where a) shows close up image of the sample and b) shows the assembled HFPEC cell.
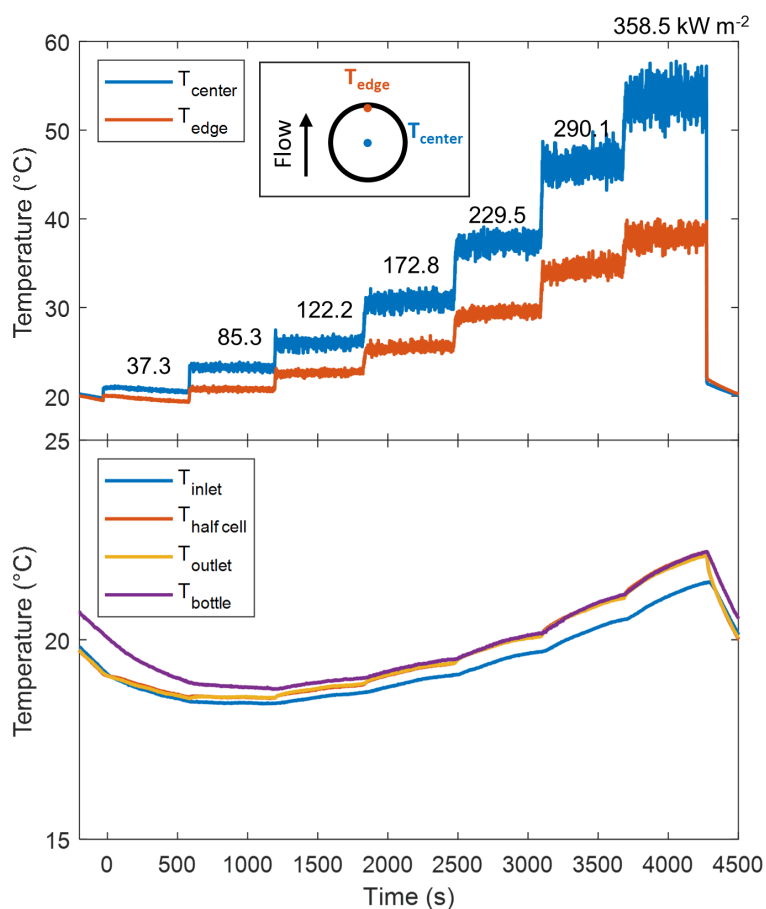

Figure S17: Temperature evolution during the high-flux tests, number above each segment indicate the irradiance used during that specific period.

13

S3.4 Fe$_2$O$_3$ cyclic voltammetry results

The complete dataset from the cyclic voltammetry under high flux for FTO|Sn−Fe$_2$O$_3$ and Ti|Sn−Fe$_2$O$_3$ is shown in Fig. S18.
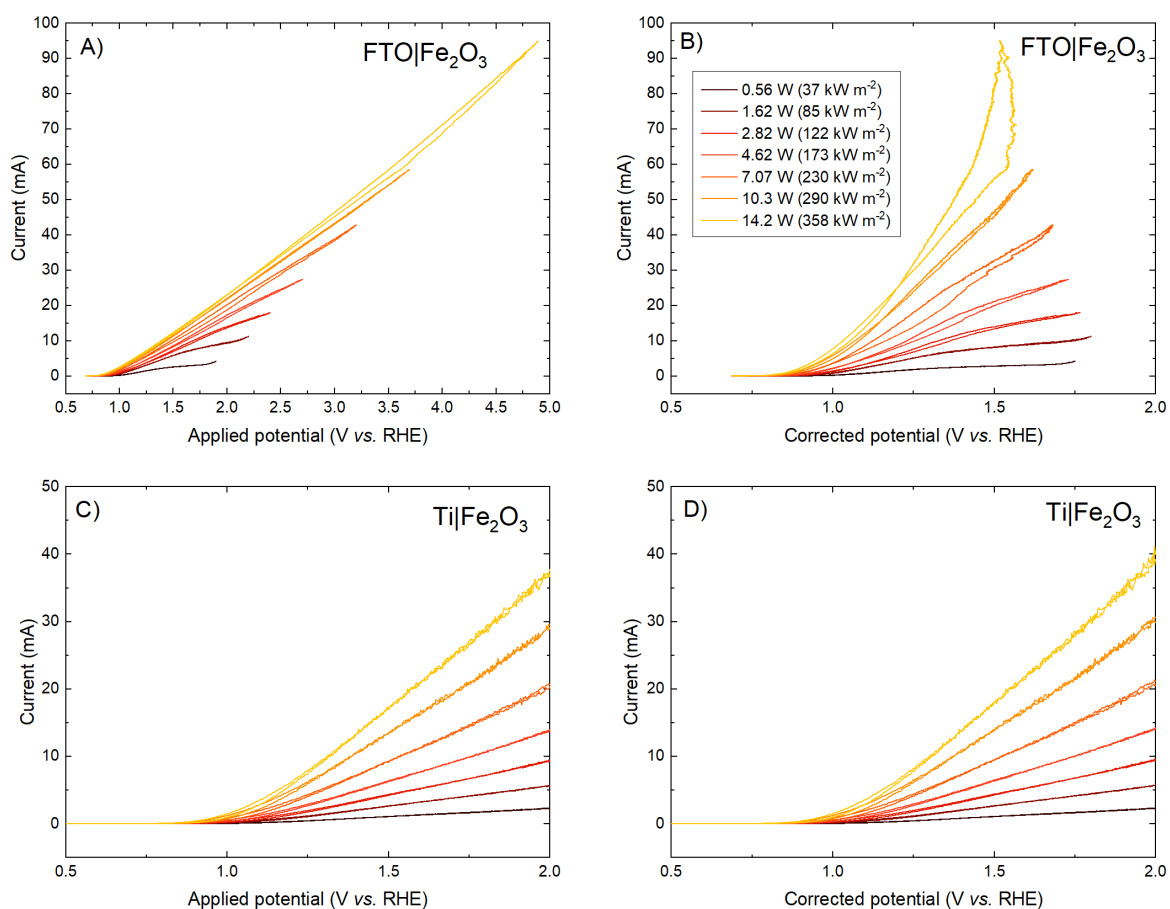

Figure S18: Raw cyclic voltammetry data under high flux for FTO|Sn−Fe$_2$O$_3$ (a,b) and Ti|Sn−Fe$_2$O$_3$ (c,d) where a) and c) show the results without ohmic drop compensation and b) and d) show the results after ohmic drop compensation.

Figure S19: Raw cyclic voltammetry data (current plotted logarithmically) under high flux for FTO|Sn−Fe$_2$O$_3$ (a,b) and Ti|Sn−Fe$_2$O$_3$ (c,d) where a) and c) show the results without ohmic drop compensation and b) and d) show the results after ohmic drop compensation.
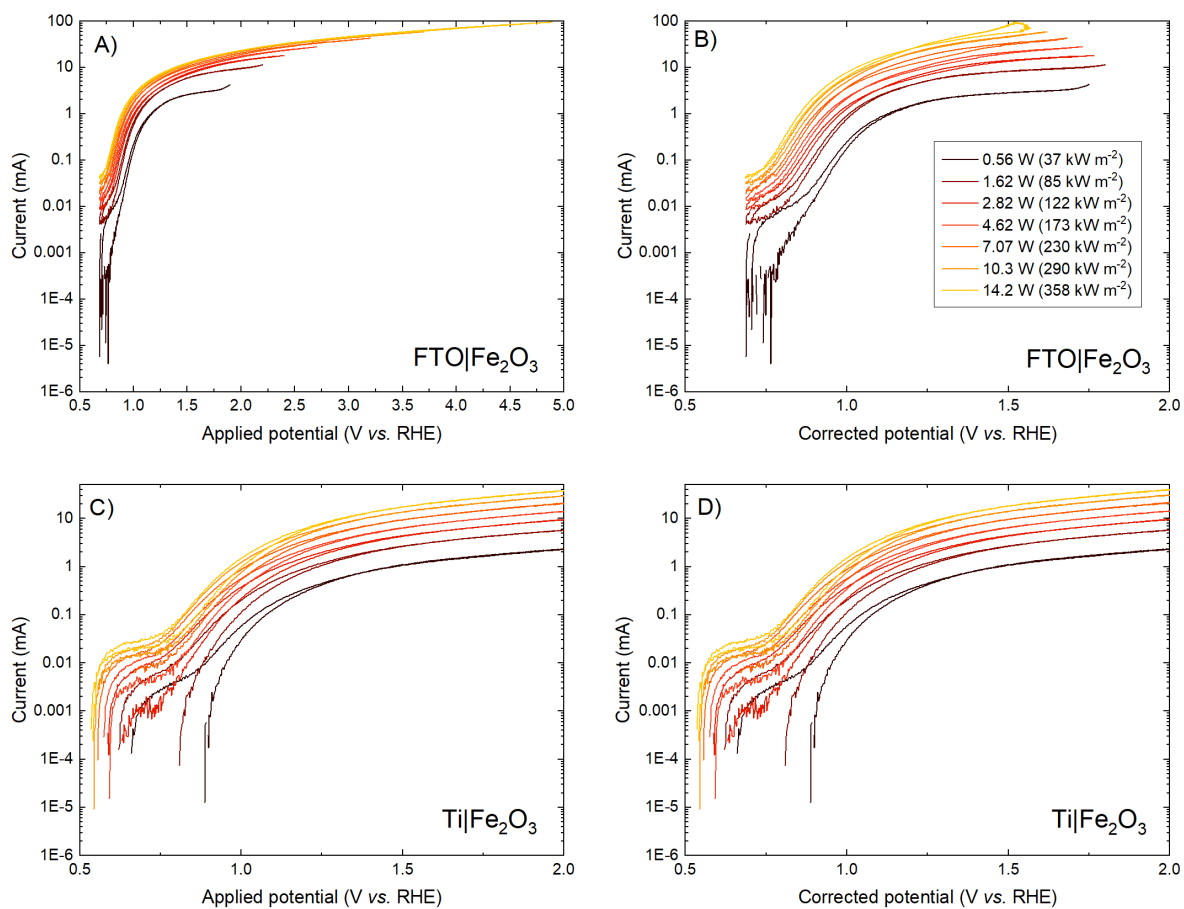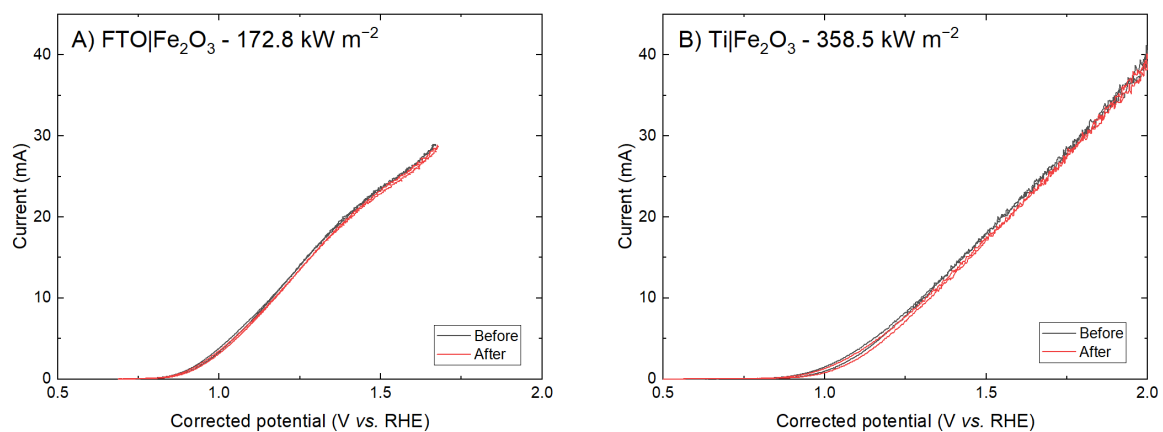
S3.5 Fe₂O₃ stability results

Figure S20: Cyclic voltammetry data under high flux for FTO|Sn−Fe$_2$O$_3$ (a) and Ti|Sn−Fe$_2$O$_3$ (b) showing the stable photoelectrochemical behaviour before and after electrochemical impedance spectroscopy.

S3.6 Behaviour of Fe$_2$O$_3$ films at different temperatures

Fig. S21 shows the photoelectrochemical behaviour of Ti|Fe$_2$O$_3$ at different temperatures. The charge transfer efficiency at the surface ($\Phi_{surface}$), calculated using chronoamperometry approach,[29] shows a known effect with temperature: it decreases at low potentials and increases at higher potential with temperature. Saturated current densities, when $\Phi_{surface} \approx 1$, increase with temperature, probably due to enhance charge transfer in the bulk of the semiconductor.
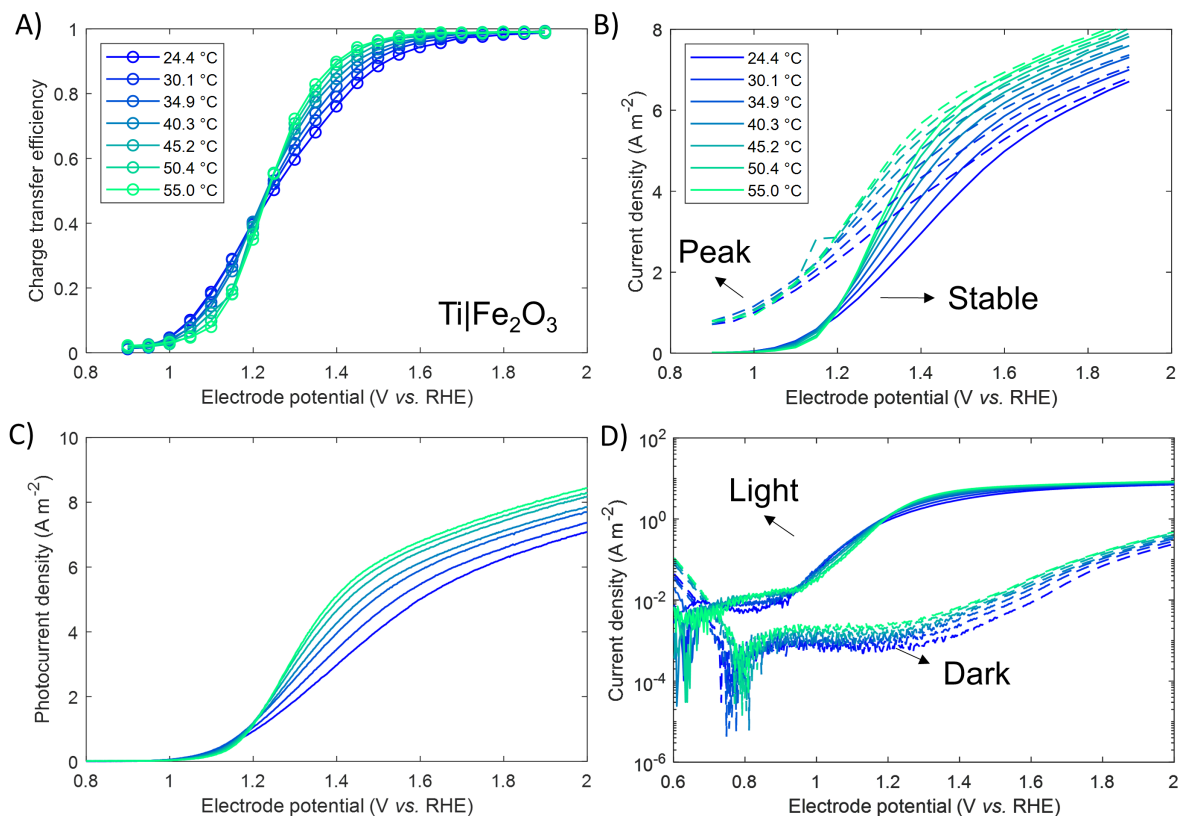

Figure S21: A) Charge transfer efficiency at the surface calculated from chronoamperometries for Ti|Fe$_2$O$_3$ in 1M NaOH at different temperatures, B) Peak and stable photocurrent (after 10 s of illumination) of corresponding chronoamperometries. C) Calculated photocurrent density ($j_{ph} = j_{light} - j_{dark}$) at different temperatures. D) Voltammograms for the same sample at different temperatures in the dark and light, current densities are logarithmic scale to observer onset potentials more clearly.

Figure S22: A) Charge transfer efficiency at the surface calculated from chronoamperometries for FTO|Fe$_2$O$_3$ in 1M NaOH at different temperatures, B) Peak and stable photocurrent of corresponding chronoamperometries. C) Calculated photocurrent density ($j_{ph} = j_{light} - j_{dark}$) at different temperatures. D) Voltammograms for the same sample at different temperatures in the dark and light, current densities are logarithmic scale to observer onset potentials more clearly.
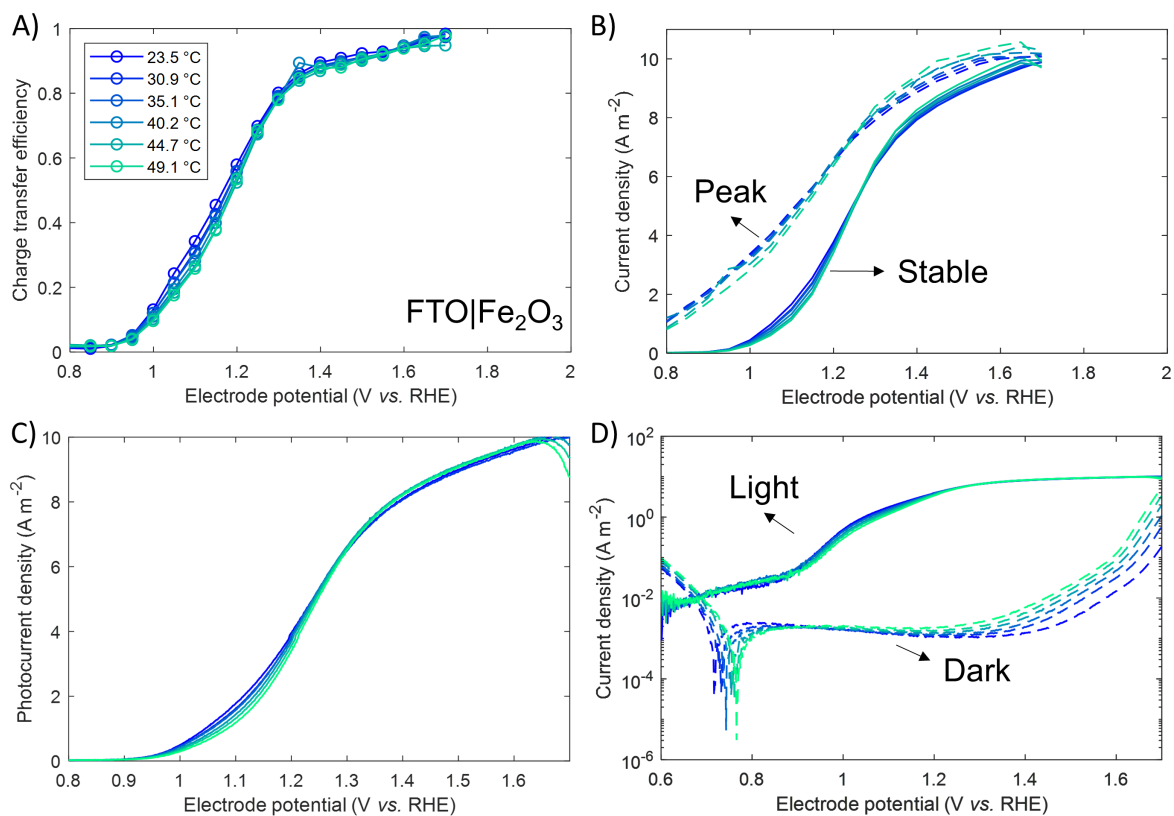
S3.7 Degradation model for BiVO$_4$ under high irradiances

The photocurrent density and corrosion rate were estimated using the Butler-Gärtner relationship. The following assumptions and definitions were necessary:

- The photoelectrode is planar and the dissolution of BiVO$_4$ is homogeneous throughout the surface, and no passivating film is formed during the degradation.

- Electron-hole recombination at the surface is negligible.

- Permittivity, volumetric mass density, flat band potential and diffusion length are constants and independent of the temperature and photon flux.

- The instantaneous corrosion rate is a function of the instantaneous photocurrent density expressed in terms of the dissolution fraction (Φ_{deg}).

- The dissolution fraction (Φ_{deg}) is not time-dependent.

Due to the film thickness decreasing with time, the Butler-Gartner relationship was defined as a step function depending on the relationships between the instantaneous film thickness (L_{film}), the diffusion length (L_p) and the space charge region (W_{SRC}), expressed as follows:

$$j_{\text{GB}} = \begin{cases} eI_0 \left(1 - \frac{\exp(-\alpha W_{\text{SCR}})}{1 + \alpha L_p}\right) & L_{\text{film}} > L_p \\ eI_0 \left(1 - \frac{\exp(-\alpha W_{\text{SCR}})}{1 + \alpha L_{\text{film}}}\right) & W_{\text{SCR}} \le L_{\text{film}} \le L_p \\ eI_0 \left(1 - \frac{\exp(-\alpha L_{\text{film}})}{1 + \alpha L_{\text{film}}}\right) & L_{\text{film}} < W_{\text{SCR}} \end{cases} \tag{3}$$
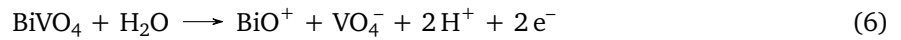
where W_{SCR} can be expressed as a function of:

$$W_{\text{SCR}} = \sqrt{\frac{2\varepsilon_r \varepsilon_0}{e n_0}(E - E_{fb})} \tag{4}$$

where α is the average absorptivity, e is the elementary charge, I_0 is the incident photon intensity, ε_r is the relative permittivity of the film, ε_0 is the vacuum permittivity, n_0 is the donor density, E is the applied potential and E_{fb} is the flat band potential.

Assuming two electrons transfer for the dissolution of BiVO$_4$ and that the formation of a passivating film is kinetically hindered,[30] the instantaneous corrosion rate can be estimated as:

$$\text{CR} = \Phi_{deg} \times \frac{j_{\text{GB}} M}{2 F \rho} = \frac{\Delta L_{\text{film}}}{\Delta t} \tag{5}$$

$$\text{BiVO}_4 + \text{H}_2\text{O} \longrightarrow \text{BiO}^+ + \text{VO}_4^- + 2\,\text{H}^+ + 2\,\text{e}^- \tag{6}$$

where Δt is the time between the current measurements, M and ρ are the molecular weight and volumetric mass density of BiVO$_4$, and Φ_{deg} is the dissolution fraction, i.e., the fraction of charge that is involved in the dissolution process. The corrosion rate (CR) has units of [length] [time]$^{-1}$ and it can be used to estimate the evolution of film thickness after Δt has passed.
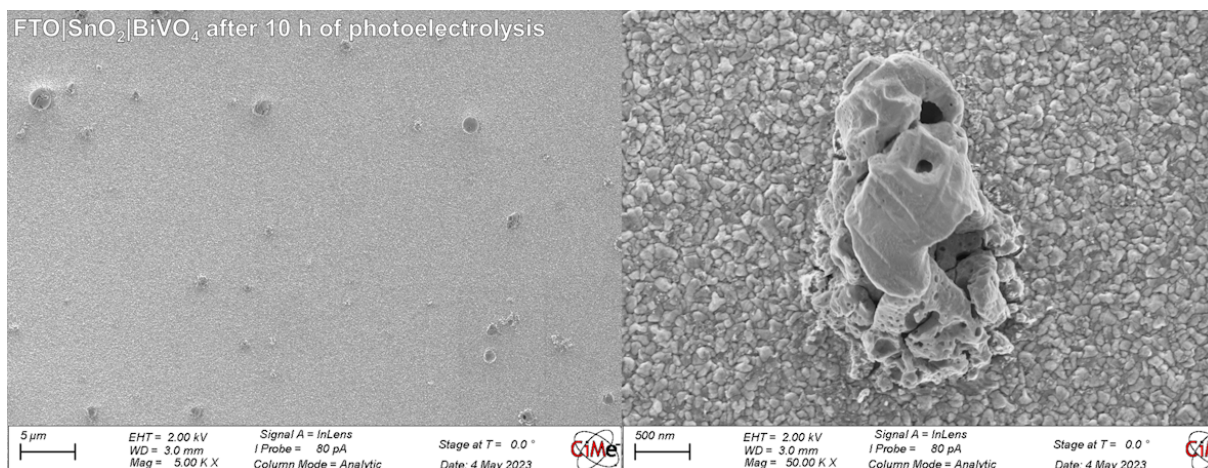
Figure S23: SEM images of FTO|SnO$_2$|BiVO$_4$ after 10 h of photoelectrolysis at 1.23 V *vs.* RHE in 1 M KPi, pH = 6.6, at room temperature (ca. 25 °C). The image on the left shows the photoelectrode with defects protruding from the surface. On the right the remnants of those defects can be observed, while the rest of the surface is exposed SnO$_2$.
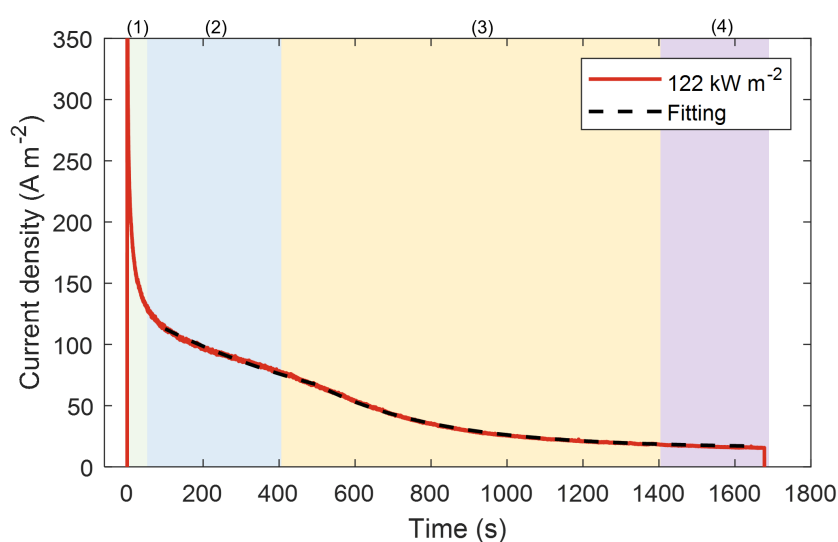

Figure S24: Transient photocurrent, identified regions for FTO|SnO$_2$|BiVO$_4$ at 1.23 *vs.* RHE in 1 M KPi, pH = 6.6, 122 kW m^{-2}.

Table S3: Time of transition between the different regions identified for transient photocurrents for FTO|SnO$_2$|BiVO$_4$ at 1.23 *vs.* RHE in 1 M KPi, pH = 6.6, at different irradiances. The transition to the stable current region (4) was estimated for a variation of 2% respect to the last recorded current (under illumination).

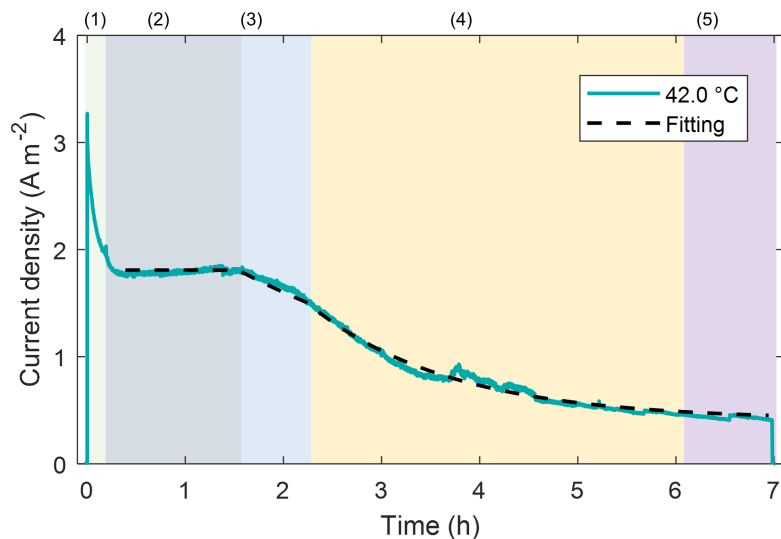| Irradiance (kW m^{-2})	Transition between regions (s)		
	(1)-(2)	(2)-(3)	(3)-(4)
122	112	490	≈1588
173	82	364	≈1542
230	64	204	≈1452
290	50	136	≈1405
358	10	42	≈1157

20

Figure S25: Transient photocurrent, identified regions for FTO|SnO$_2$|BiVO$_4$ at 1.23 *vs.* RHE in 1 M KPi, pH = 6.6, at 42 °C under 1 sun illumination.

Table S4: Time of transition between the different regions identified for transient photocurrents for FTO|SnO$_2$|BiVO$_4$ at 1.23 *vs.* RHE in 1 M KPi, pH = 6.6, at different temperatures under 1 sun illumination. The transition to the stable current region (5) was estimated for a variation of 2% respect to the last recorded current (under illumination).

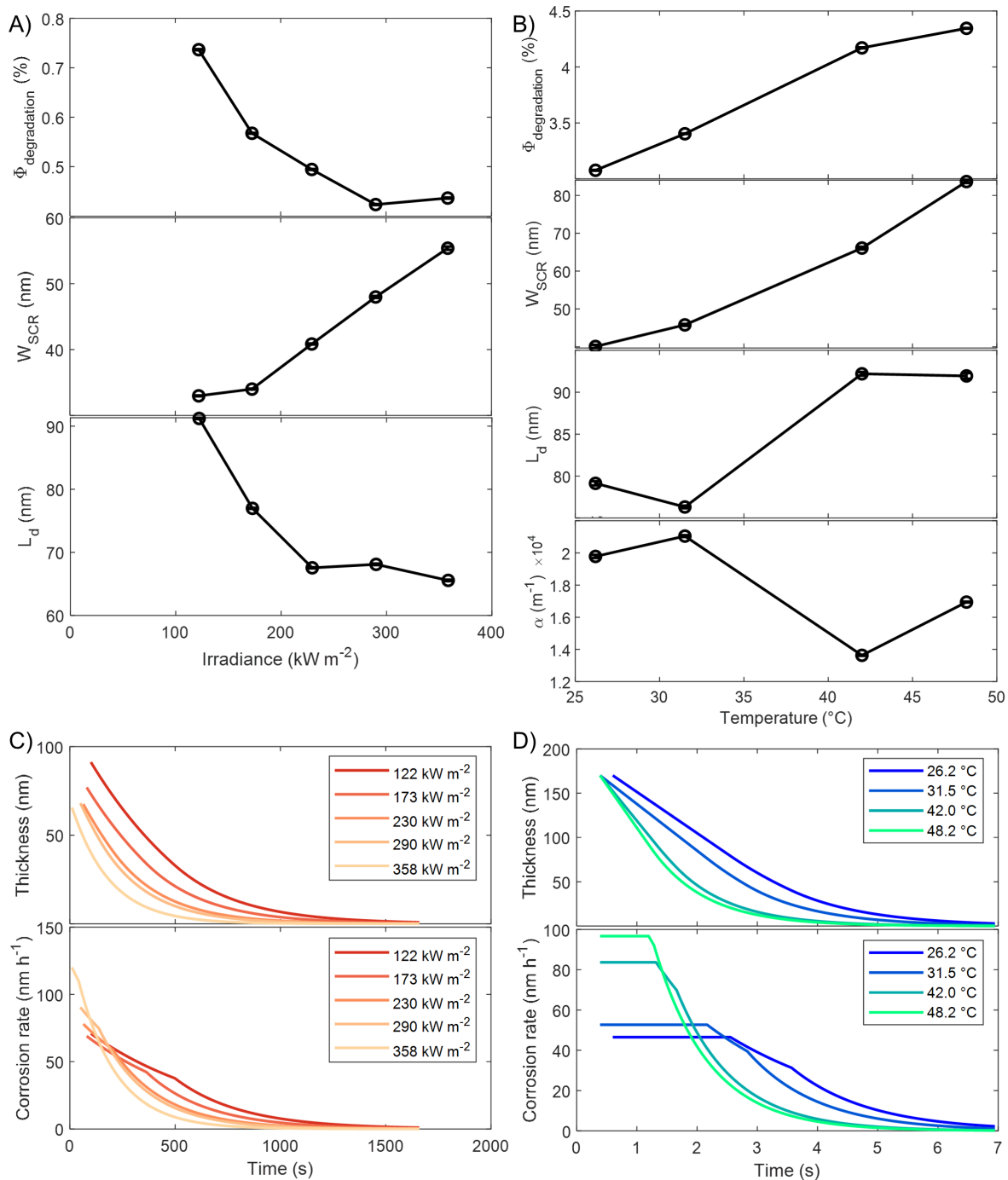| Temperature (°C)	Transition between regions (h)			
	(1)-(2)	(2)-(3)	(3)-(4)	(4)-(5)
26.2	≈ 0.6	2.5	3.5	≈ 6.8
31.5	≈ 0.4	2.0	2.6	≈ 6.5
42	≈ 0.4	1.7	2.2	≈ 6.6
48.2	≈ 0.4	1.3	1.4	≈ 6.2

Figure S26: Fitted parameters for transient photocurrent for FTO|SnO$_2$|BiVO$_4$ at 1.23 *vs.* RHE in 1 M KPi, pH = 6.6, at different irradiances (A) and temperatures under 1 sun illumination (B). Predicted evolution of BiVO$_4$ film thickness and instantaneous dissolution rates for different irradiances (C) and different temperatures (D).
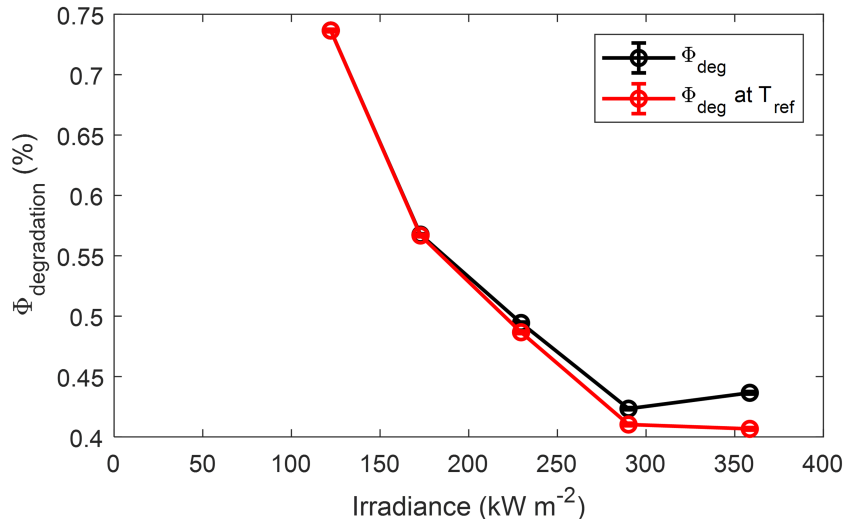
Figure S27: The degradation fraction Φ_{deg} as a function of irradiance before and after accounting for temperature effects on W_{SCR} and L_{d}, the temperature at the lowest irradiance (21.5 °C for 122 kW m^{-2}) was used as reference.
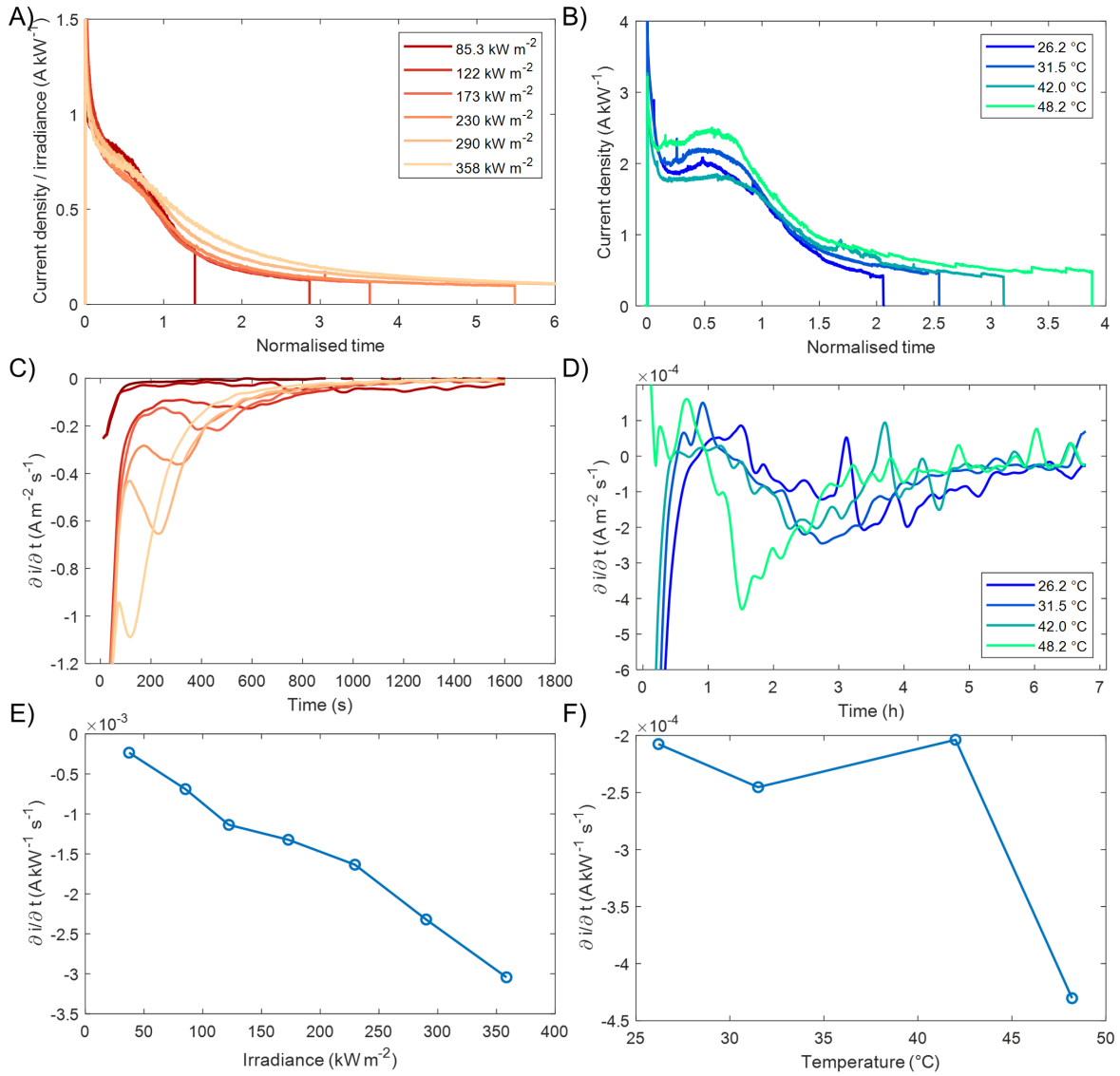
Figure S28: Normalised photocurrent by irradiance for FTO|SnO$_2$|BiVO$_4$ at 1.23 *vs.* as a function of normalised time respect to the time of highest photocurrent decay, at different (A) irradiances and (B) temperatures under 1 sun illumination. (C,D) Derivative of the current density vs time at different irradiances and temperatures as a function of time, (E,F) and maximum decay of (photocurrent density / irradiance) as a function of irradiance and temperature.

References

[1] O. Khaselev and J. A. Turner, *Science*, 1998, **280**, 425–427.

[2] G. Peharz, F. Dimroth and U. Wittstadt, *International Journal of Hydrogen Energy*, 2007, **32**, 3248–3252.

[3] H. Wang, T. Deutsch and J. A. A. Turner, *ECS Transactions*, 2008, **6**, 37–44.

[4] C. K. Ong, S. Dennison, K. Hellgardt and G. Kelsall, *ECS Transactions*, 2011, **35**, 11–19.

[5] S. Bell, G. Will and J. Bell, *International Journal of Hydrogen Energy*, 2013, **38**, 6938–6947.

[6] S. Rau, S. Vierrath, J. Ohlmann, A. Fallisch, D. Lackner, F. Dimroth and T. Smolinka, *Energy Technology*, 2014, **2**, 43–53.

[7] M. R. Shaner, K. T. Fountaine, S. Ardo, R. H. Coridan, H. A. Atwater and N. S. Lewis, *Energy Environ. Sci.*, 2014, **7**, 779–790.

[8] S. A. Bonke, M. Wiechen, D. R. MacFarlane and L. Spiccia, *Energy & Environmental Science*, 2015, **8**, 2791–2796.

[9] A. Nakamura, Y. Ota, K. Koike, Y. Hidaka, K. Nishioka, M. Sugiyama and K. Fujii, *Applied Physics Express*, 2015, **8**, 107101.

[10] X. Ye, J. Yang, M. Boloor, N. A. Melosh and W. C. Chueh, *Journal of Materials Chemistry A*, 2015, **3**, 10801–10810.

[11] J. Jia, L. C. Seitz, J. D. Benck, Y. Huo, Y. Chen, J. W. D. Ng, T. Bilir, J. S. Harris and T. F. Jaramillo, *Nature Communications*, 2016, **7**, 13237.

[12] G. Segev, H. Dotan, K. D. Malviya, A. Kay, M. T. Mayer, M. Grätzel and A. Rothschild, *Advanced Energy Materials*, 2016, **6**, 1500817.

[13] A. Fallisch, L. Schellhase, J. Fresko, M. Zedda, J. Ohlmann, M. Steiner, A. Bösch, L. Zielke, S. Thiele, F. Dimroth and T. Smolinka, *International Journal of Hydrogen Energy*, 2017, **42**, 26804–26815.

[14] A. Vilanova, T. Lopes, C. Spenke, M. Wullenkord and A. Mendes, *Energy Storage Materials*, 2018, **13**, 175–188.

[15] A. Vilanova, T. Lopes and A. Mendes, *Journal of Power Sources*, 2018, **398**, 224–232.

[16] Y. Bicer and I. Dincer, *International Journal of Hydrogen Energy*, 2018, **43**, 10258–10267.

[17] S. Tembhurne, F. Nandjou and S. Haussener, *Nature Energy*, 2019, **4**, 399–407.

[18] M. V. N. S. Gupta, H. Baig, K. S. Reddy, T. K. Mallick, B. Pesala and A. A. Tahir, *ACS Applied Energy Materials*, 2020, **3**, 9002–9009.

[19] M. A. Khan, I. Al-Shankiti, A. Ziani, N. Wehbe and H. Idriss, *Angewandte Chemie*, 2020, **132**, 14912–14918.

[20] A. Vilanova, P. Dias, J. Azevedo, M. Wullenkord, C. Spenke, T. Lopes and A. Mendes, *Journal of Power Sources*, 2020, **454**, 227890.

[21] X. Xing, S. Tang, H. Hong and H. Jin, *International Journal of Hydrogen Energy*, 2020, **45**, 9612–9623.

[22] P. Zhou, I. A. Navid, Y. Ma, Y. Xiao, P. Wang, Z. Ye, B. Zhou, K. Sun and Z. Mi, *Nature*, 2023, **613**, 66–70.

[23] I. Holmes-Gentle, S. Tembhurne, C. Suter and S. Haussener, *Nature Energy*, 2023, 586–596.

[24] R. Bader, L. Schmidt, S. Haussener and W. Lipiński, Light, Energy and the Environment, Canberra, 2014, p. RW4B.4.

[25] G. Levêque, R. Bader, W. Lipiński and S. Haussener, *Optics Express*, 2016, **24**, A1360.

[26] F. Bedoya-Lora, A. Hankin, I. Holmes-Gentle, A. Regoutz, M. Nania, D. Payne, J. Cabral and G. Kelsall, *Electrochimica Acta*, 2017, **251**, 1–11.

[27] F. F. Abdi, T. J. Savenije, M. M. May, B. Dam and R. van de Krol, *The Journal of Physical Chemistry Letters*, 2013, **4**, 2752–2757.

[28] R. Gill, E. Bush, P. Haueter and P. Loutzenhiser, *Review of Scientific Instruments*, 2015, **86**, 125107.

[29] F. E. Bedoya-Lora, M. E. Valencia-García, A. Hankin, D. Klotz and J. A. Calderón, *Electrochimica Acta*, 2022, **402**, 139559.

[30] F. M. Toma, J. K. Cooper, V. Kunzelmann, M. T. McDowell, J. Yu, D. M. Larson, N. J. Borys, C. Abelyan, J. W. Beeman, K. M. Yu, J. Yang, L. Chen, M. R. Shaner, J. Spurgeon, F. A. Houle, K. A. Persson and I. D. Sharp, *Nature Communications*, 2016, **7**, 12012.